IEICE TRANS. COMMUN., VOL.E87–B, NO.4 APRIL 2004

PAPER

Experimental Study of Non-specular Wave Scattering from Building Surface Roughness for the Mobile Propagation Modeling

Hary BUDIARTO[†a)], **Kenshi HORIHATA**[†], **Katsuyuki HANEDA**[††], ***Student Members***, ***and*** **Jun-ichi TAKADA**[††b)], ***Member***

SUMMARY In the urban area, buildings are the main scatterer which dominate the mobile propagation characteristics. However, reflection, diffraction, and scattering on the building surfaces in the radio environment induce undesirable multipath propagation. Multipath prediction with respect to a building surface has been conventionally based on an assumption that reflection from the surface has a substantial specular direction. However non-specular scattering from the building surface can affect the channel characteristics as well as specular scattering. This paper presents multipath characteristics of non-specular wave scattering from building surface roughness based on the experimental results. Superresolution method was applied as an approach to handle the signal parameters (DoA, ToA) of the individual incoming waves reflected from building surface roughness. The results show that the multipaths can be detected at many scatterers, such as ground, window's glass, window's frames and bricks surface, as well as directly from the transmitter. Most of the scattered waves are arriving closely from specular directions. The measured reflection coefficients were well bounded by reflection coefficients of the theoretically smooth and random rough surface. The Fresnel reflection coefficient formula, considering the finite thickness of the building surface and Gaussian scattering correction, give better prediction for glass and bricks reflection coefficient measurement.

key words: *mobile propagation, surface roughness, non-specular scattering, signal processing, ESPRIT*

1. Introduction

Wireless personal communication systems have been continuously developing worldwide. These systems have also been extended to complex environments, such as urban and indoor microcells. In urban areas, buildings are the dominant scatterers determining propagation properties. The propagation prediction must reliably predict the influence of buildings and other obstructions. Microscopic scattering models are required to reflect the properties of the environmental objects. If they are not adequately modeled, the propagation prediction can result in large errors [9]. On the other hand, reflection, diffraction, and scattering of the electromagnetic waves on the building surfaces in the radio environment induce undesirable multipath propagation. Consequently, the transmitted signal reaches the receiver through different propagation paths. Multipath prediction on a building surface was conventionally based on an assumption that reflection from the surface has a substantial specular reflection [2], [10]. However, the multipaths are also generated by scattered waves propagating in non-specular directions. Therefore, non-specular scattering from the building surface can also affect the channel characteristics as well as specular scattering [1]. In order to predict the channel characteristic in more detail, multipath propagation of microscopic scattering is important. For the demonstration of these effects, some researchers have assumed the scattering to follow Lamberts' law [10], which is applicable to the surface roughness characterized by random deviation of the surface height. Unfortunately, the above assumption does not seem to be applicable on the scattering from building surfaces, whose windows and other architectural features have fair structures.

This paper presents multipath characteristics of non-specular wave scattering from the building surface roughness based on experimental results. The antenna element was scanned spatially to detect the directions of arrival (DoA) and the carrier frequency was scanned to obtain the times of arrival (ToA). Superresolution method was applied as an approach to handle the signal parameters (DoA, ToA) of the individual incoming waves scattered from building surface roughness. In order to comprehend the microscopic mechanism of scattering, the signal parameters are to be incorporated into the geometrical ray-tracing. Two models of the spatial scanning were applied to predict multipath characteristics in more detail for periodic structures. The results show that the multiple paths can be detected at many scatterers, such as ground, window's glass, window's frames, bricks surface, as well as directly from the transmitter. The signal parameters of the arrival waves from the building scatterer have a tendency to be distributed around the angle of specular direction. It was also shown that the glass and bricks reflection coefficients were well bounded by the theoritical Fresnel reflection formulas for smooth surfaces and rough surfaces using the scattering correction of the modified Gaussian rough surface [3]. Moreover, the Fresnel reflection coefficient formula with finite thickness of the building surface [4] and the modified Gaussian scattering correction give better prediction when applied to glass and bricks surfaces.

Manuscript received May 26, 2003.
Manuscript revised September 7, 2003.

[†]The authors are with the Department of Electrical & Electronic Engineering, Tokyo Institute of Technology, Tokyo, 152-8552 Japan.
[††]The authors are with the Department of International Development Engineering, Tokyo Institute of Technology, Tokyo, 152-8552 Japan.
a) E-mail: hary@ap.ide.titech.ac.jp
b) E-mail: takada@ap.ide.titech.ac.jp

2. Environment Consideration

2.1 Building Surface Profile

The profile of the building surface is shown in Fig. 1. The profile was taken from one of the buildings at Tokyo Institute of Technology. The surface of the building has non-uniformity due to the windows (glass), frames (aluminum), and walls (bricks). The surface has periodical irregularity of five periods. One period of the surface equals 3.7 m. The windows are made up of the sidewall, aluminum frames and plain glasses, which in principle are the building roughness, as well as the wall surface. The dimensions of the window's glasses of the building are $0.85 \times 1.5\,\mathrm{m}^2$, $0.8 \times 1.5\,\mathrm{m}^2$, and $0.85 \times 1.5\,\mathrm{m}^2$. The three different window frames have outer dimensions of $0.04 \times 1.5\,\mathrm{m}^2$, $0.05 \times 1.5\,\mathrm{m}^2$ and $0.10 \times 1.5\,\mathrm{m}^2$. The first and the third window frames have the same offset depth of 0.16 m different from the second window frame that has 0.12 m offset depth. The windows are elevated 1.5 m from the ground. The wall surface, that has periodical roughness in both horizontal and vertical directions, is made of $0.1 \times 0.05\,\mathrm{m}^2$ bricks with 0.01 m gap among each other.

2.2 Transmitter and Receiver Models

The transmitter and receiver antennas were linearly polarized rectangular microstrip antennas with ground plane size of $0.08 \times 0.08\,\mathrm{m}^2$. The patch size was $0.0179 \times 0.0179\,\mathrm{m}^2$ on a dielectric substrate with $\epsilon_r = 2.55$. The center frequency of the antennas was 4.95 GHz with bandwidth of 180 MHz. The wavelength was comparable with or smaller than depth of building surface roughness. The receiver antenna was shifted spatially by a X-Y positioner to obtain field strength at each point in the scanning region. Both antennas were aligned to transmit and receive vertical polarization. The height of the transmitter antenna was 1.9 m from ground. The transmitter antenna was fixed at 2.7 m away in front of the building surface. Figure 2 shows the arrangement of the experiment [6]. The transfer function between transmitter and receiver antennas was measured using a Vector Network Analyzer (VNA). The X-Y positioner was used for automatic scanning of the receiver antenna. The measurement of the frequency characteristics of the transfer function and the shifting of receiver antenna were operated automatically using a personal computer through the positioner controller and General Purpose Interface Bus (GPIB) to achieve high accuracy and easy measurement. The X-Y positioner has an accuracy of 1 mm. Table 1 shows the detailed parameters of the experiments.

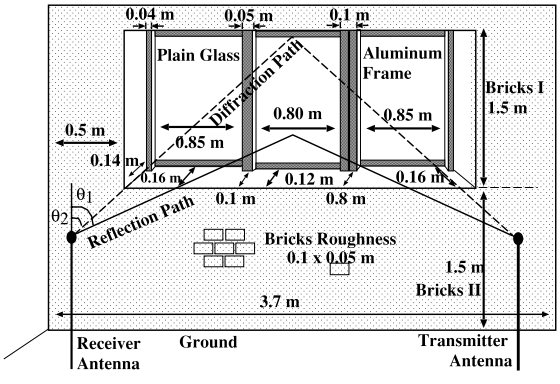

Fig. 1 Building the surface profile.

2.3 The Spatial Scanning Model

The spatial scanning was configured to resemble an array antenna, also called synthesized uniform rectangular array (URA). The measurement points during the spatial scanning were discretized for every 0.025 m toward the horizontal and vertical directions. The measurement was performed along 0.5 m in the vertical direction. The middle of the vertical direction scanning region was at the same height as the transmitter antenna. Figure 3 illustrates two models of the spatial scanning. Model I performs the measurement 8.125 m along the horizontal direction. The transmitter antenna is positioned facing towards the bricks' surface of the building. The first vertical direction of measurement is 0.7 m away from the transmitter antenna, which corresponds to 10° in-

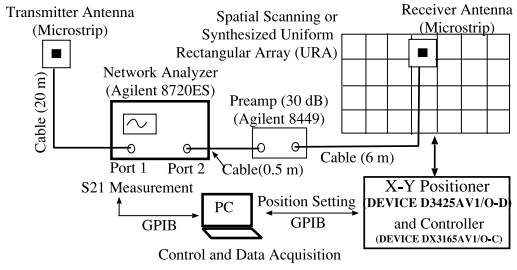

Fig. 2 Equipment arrangement.

Table 1 Experimental parameter.

Antennas	Tx & Rx Microstrip Reflection coefficient is bellow −10 dB in 4.85–5.05 GHz. Beam width in E and H planes are 45°
Measurement Points	Spatially 10 × 10 points (25 mm interval), 21 points over frequency (4.85–5.05 GHz).
Snapshot	20 times
Estimations Parameters	The number of waves and each wave's azimuth, elevation, delay and path gain
Signal processing	LS 3-D Unitary ESPRIT
Smoothing in ESPRIT	Spatially 4 times and 7 times over frequency
Wave Polarization	Vertical-Vertical
Normalization	Face-to-face, the distance between Tx and Rx is 1 m at experiment location

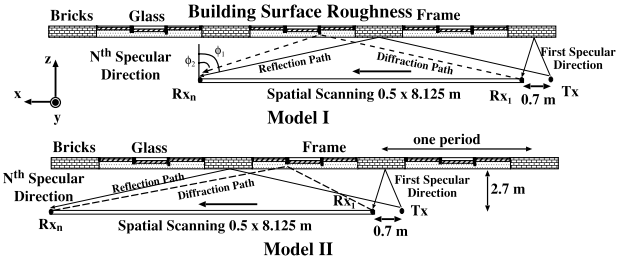

Fig. 3 Top view of the spatial scanning model.

cident angle in the specular direction. In the case of Model II, the transmitter antenna is positioned facing towards the bricks' surface of another period. Measurement parameters of model II were the same as for model I. The purpose of this setup is to investigate in more detail the multipath characteristics affected by the periodical structure of the building surface.

2.4 Calibration System

Since the VNA also measures the transfer functions of the cable and amplifier, calibration of the data measurement system is required to eliminate the effect of the equipment. The transfer function of the signal was measured using a network analyzer with the frequency range from 4.85 to 5.05 GHz. The transfer function measured by the VNA can be expressed as follows.

$$X(f) = H(f) \times G(f) \tag{1}$$

where $G(f)$ is the transfer function of the cable, amplifier and antenna complex directivity at broadside, and $H(f)$ is the Friis free space transfer function, which is given as,

$$H(f) = \frac{\lambda}{4\pi d} \exp\left(-j\frac{2\pi}{\lambda}d\right) \tag{2}$$

where d is the propagation path, and λ is the wavelength. All measurement data resulted from this experiment was already calibrated by applying function $G(f)$, which was obtained from the measurement using the transmitter and receiver antennas positioned face-to-face with 1 m distance from each other, in an open space.

3. Reflection Coefficient

3.1 Fresnel Reflection Formula for Semi-Infinite Medium

The Fresnel models presented here assume a homogeneous dielectric material semi-infinite in extent. Although this is not true for real buildings, the dimensions of the building surface are sufficiently large that it may be approximated as infinite. The Fresnel reflection coefficient (Γ) relates the field reflected from infinite dielectric material to the incident field as,

$$E_{\perp}^{r} = \Gamma_{\perp} E_{\perp}^{i} \tag{3}$$

where $E_{\perp}^{i}$ and $E_{\perp}^{r}$ are the incident and reflected fields, respectively. The subscript $\perp$ corresponds to the vertical polarization, i.e. electric field is perpendicular to incidence plane. As the vertical polarization is used in the measurement, horizontal polarization is not considered. The reflection coefficients, determined by material properties, angle of incidence (θ_i) and frequency, are given by

$$\Gamma_{\perp} = \frac{\eta_2 \cos\theta_i - \eta_1 \cos\theta_t}{\eta_2 \cos\theta_i + \eta_1 \cos\theta_t}, \tag{4}$$

where the wave impedance (η_m) and the transmitted wave angle (θ_t) are expressed as

$$\eta_m = \sqrt{\frac{j\omega\mu_m}{\sigma_m + j\omega\epsilon_m}} \quad (m = 1, 2), \tag{5}$$

$$\cos\theta_t = \sqrt{1 - \left(\frac{k_1}{k_2}\right)^2 \sin^2\theta_i}, \tag{6}$$

where ω is the radian frequency and the wavenumbers (k_m) are

$$k_m = \omega\sqrt{\mu_m\epsilon_m - \frac{j\mu_m\sigma_m}{\omega}}. \tag{7}$$

The properties of each of the dielectric materials at the interface are characterized by their permitivity (ϵ_m), magnetic permeability (μ_m), and conductivity (σ_m).

3.2 Fresnel Reflection Formula for Finite Thickness Medium

Assuming that the medium is flat with finite thickness, the reflection coefficient R of the medium can be expressed as

$$R_{\perp} = \frac{1 - \exp(-j2\delta)}{1 - \Gamma_{\perp}^2 \exp(-j2\delta)}\Gamma_{\perp}, \tag{8}$$

$$\delta = \frac{2\pi d}{\lambda}\sqrt{\eta_2^2 - \sin^2\theta_i}, \tag{9}$$

where d is the thickness of the material, and $\Gamma_{\perp}$ is given by Eq. (4).

3.3 Gaussian Scattering Loss Factor

The Rayleigh criterion is commonly used as a test for surface roughness, giving the critical height (h_c) of surface protuberances as,

$$h_c = \frac{\lambda}{8\cos\theta_i} \tag{10}$$

where λ is the wavelength. The heigth of a rough surface h is defined as the minimum to maximum surface protuberance, as shown in Fig. 2. A surface is considered smooth if $h < h_c$ and is rough if $h > h_c$. Equation (10) shows that as the incident angle approaches grazing, the critical height becomes larger, effectively reducing the scattering effect of the surface protuberances. For the case of rough surfaces, a

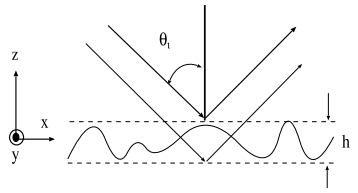

Fig. 4 Surface roughness protuberances.

scattering loss factor (ρ_s) can be derived to account for diminished energy in the specular direction of reflection, given by,

$$\rho_s = \exp\left[-8\left(\frac{\pi\sigma_h \cos\theta_i}{\lambda}\right)^2\right] \tag{11}$$

where σ_h is the standard deviation of the surface height about the mean surface height in the first Fresnel zone of the illuminating antenna. The assumption in the above equation is that the surface height is Gaussian distributed. In general, incident radiation on a surface will induce a current density J which is a function of both the x and z directions shown in Fig. 4. Equation (11) assumes that this surface current density at height z is always $J(z)$, regardless of whether the surface element at a particular x is shadowed or illuminated by another part of the surface. This approximation was made to simplify the integral equations used to derive Eq. (11). With ρ_s used to modify the reflection coefficients, this model hence can be called as the Gaussian rough surface scattering model, which is written as

$$(\Gamma_\perp)_s = \rho_s \Gamma_\perp. \tag{12}$$

It was reported in [4] that the scattering loss factor of Eq. (11) gives better agreement with measured results when modified as,

$$\rho_s = \exp\left[-8\left(\frac{\pi\sigma_h \cos\theta_i}{\lambda}\right)^2\right] I_o\left[8\left(\frac{\pi\sigma_h \cos\theta_i}{\lambda}\right)^2\right] \tag{13}$$

where $I_o(z)$ is the modified Bessel function of zeroth order. When the argument of the modified Bessel function is small, Eqs. (11) and (13) are approximately equal, since $I_o(z)$ approaches unity.

4. Signal Processing

In order to obtain signal parameters of the arrival wave, measurement data are formulated. Suppose that L waves are impinging at the receiver have three parameters of azimuth angle ($\phi_l - \frac{\pi}{2}$), elevation angle ($\frac{\pi}{2} - \theta_l$) and delay time τ_l, where $1 \le l \le L$. With the X-Y positioner, the receiver antenna performs spatial scanning both in the horizontal and vertical directions where the intervals of the sampling points are Δ_x and Δ_y. The numbers of sampling points are M_1 and M_2, respectively. At each sampling point, it carries out M_3 points of sampling over the frequency where the interval of sampling is Δ_f and the center frequency is f_c. If the electrical lengths of the aperture of the array, $\frac{2\pi}{\lambda_c} M_1 \Delta_x$ and $\frac{2\pi}{\lambda_c} M_2 \Delta_y$, are both sufficient to be assumed as constant within the bandwidth $M_3\Delta_f$, i.e, $M_1\Delta_x \cdot M_3\Delta_f \ll c$, and $M_2\Delta_y \cdot M_3\Delta_f \ll c$, where c is a light velocity, then the measured data y_{k_1,k_2,k_3} can be expressed as,

$$z_{k_1,k_2,k_3} = \sum_{l=1}^{L}\left[s_l \prod_{r=1}^{3} e^{j\mu_l^{(k_r)}}\right] + n_{k_1,k_2,k_3} \tag{14}$$

where $0 \le k_r \le (M_r - 1)$ $1 \le r \le 3$ indicates a location of each sampling point, n_{k_1,k_2,k_3} is a white Gaussian noise of zero mean, s_l is a complex amplitude of the l^{th} wave at a reference point and $\mu_l^{(r)}$ is denoted by

$$\mu_l^{(1)} = \frac{2\pi}{\lambda_c}\Delta_x \sin\left(\phi_l - \frac{\pi}{2}\right)\cos\left(\frac{\pi}{2} - \theta_l\right), \tag{15}$$

$$\mu_l^{(2)} = \frac{2\pi}{\lambda_c}\Delta_y \sin\left(\frac{\pi}{2} - \theta_l\right), \tag{16}$$

$$\mu_l^{(3)} = 2\pi\Delta_f \tau_l. \tag{17}$$

These values include parameters of the incident waves so that the objective is to obtain these L sets of 3-D mode parameters. Then, vectorization of data measurement can be defined as

$$\begin{aligned} \boldsymbol{z} &= [z_{1,1,1}\ z_{2,1,1} \cdots z_{M_1,1,1}\ \ z_{1,2,1} \cdots \\ &\quad z_{M_1,M_2,1}\ z_{1,1,2} \cdots z_{M_1,M_2,M_3}]^T \in C, \\ &= \boldsymbol{A}\boldsymbol{s} + \boldsymbol{n}, \end{aligned} \tag{18}$$

where $s \in C^L$ and $n \in C^M$ ($M = M_1M_2M_3$) are the complex amplitude vector and noise vector respectively. The multidimensional mode matrix $\boldsymbol{A} \in C^{M\times L}$ is generated by mode matrices each of which corresponds to a parameter as

$$\boldsymbol{A} = \boldsymbol{A}(\mu^{(3)}) \diamond \boldsymbol{A}(\mu^{(2)}) \diamond \boldsymbol{A}(\mu^{(1)}) \in C^{M\times L}, \tag{19}$$

where $\diamond$ denotes the kronecker product of each row of the matrices and

$$\boldsymbol{A}(\mu^{(r)}) = [\boldsymbol{a}(\mu_1^{(r)}) \ldots \boldsymbol{a}(\mu_L^{(r)})] \in C^{M_r\times L}, \tag{20}$$

$$a(\mu_1^{(r)}) = [1\ e^{-j\mu_r^{(r)}} \ldots e^{-j(M_r-1)\mu^{(r)}}]^T \in C^{M_r}. \tag{21}$$

The 3D unitary ESPRIT algorithm [7], [8] was used to obtain the signal parameters. It is a superresolution direction finding method of the arrival wave. In physical terms, the ESPRIT is equivalent to finding out the parameters of the arrival wave using the phase difference between groups of uniformly positioned elements of sensor array. The ESPRIT array data had a size of (10×10) or (25×25) cm^2 for each observation point. The arrival wave analyses were performed at 60 observation points with an interval of 12.5 cm.

5. Signal Parameters of Arrival Waves

The signal parameters of the arrival waves that can be obtained using ESPRIT are azimuth angle, elevation angle, delay time and power. If the azimuth and elevation angles of the arrival wave are known, then the propagation path

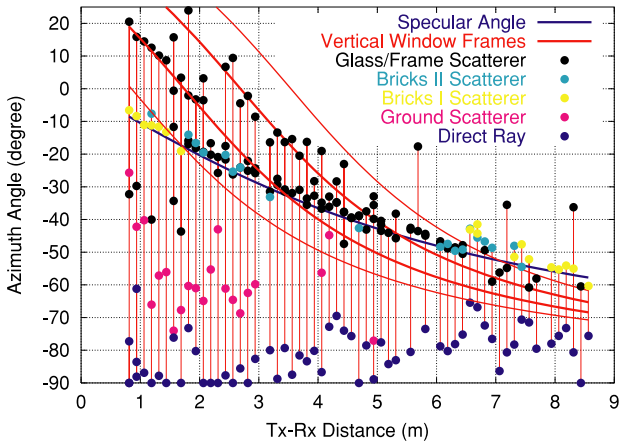

Fig. 5 Azimuth angle of arrival wave for model I.

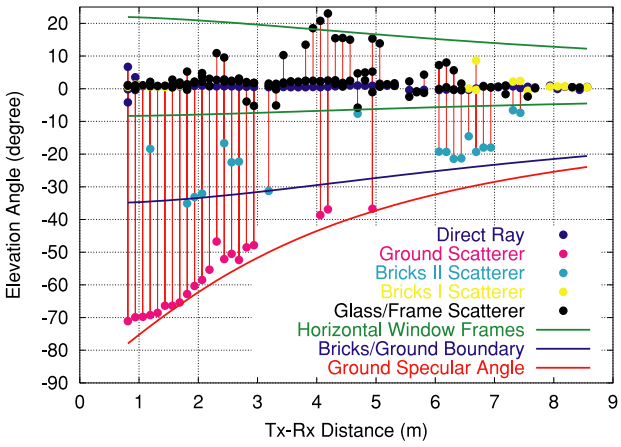

Fig. 6 Elevation angle of arrival wave for model I.

from the transmitter to the receiver antenna can be determined. Therefore, the delay time based on free space velocity (3×10^8 m/s) of each propagation path can be easily obtained. Additionally, by knowing difference between the delay time estimated by using ESPRIT result and the delay time estimated by using DoA result and free space velocity for each of the arrival waves, double scattering can be distinguished. Azimuthal and elevation angles of specular reflection point, specular diffraction point and diffuse scattering point are required for detailed classification of typical paths. The specular diffraction satisfies the Keller's law of diffraction, while a scattered wave is classified as diffuse scattering, if it is neither classified as specular reflection nor specular diffraction. The elevation and azimuth for the typical path of specular reflection and specular diffraction are shown in Figs. 1 and 3, respectively.

5.1 The Directions of Arrival Waves

Figure 5 shows the ESPRIT result for an azimuthal angle of the arrival wave. The line perpendicular to the x-axis depicts the range value of the azimuthal angle. The negative azimuthal angle, representing the wave, comes from the right-hand side of the receiver or source side (see Fig. 3). The legends in Fig. 5 show the type of scatterers. The number of icons on the vertical line corresponds to the number of multipath signals. Multiple paths can be detected from many scatterers, such as ground, window's glass or window's frames, bricks I, bricks II and directly from the transmitter. However, the ESPRIT result is not accurate enough to distinguish between the arrival waves coming from window's glass, window's frame and boundary of window's glass and frame. Therefore, they are called altogether as glass/frame scatterer. The types of brick scatterer are distinguished as the brick scatterer with height between the lower and upper part of the windows, classified as bricks-I, and the brick scatterer with height below the windows, classified as bricks-II. With respect to the scattered waves at the building surface, most of the arrival waves from window's glass and bricks I are specular reflection. This is because the azimuthal angles have a tendency to be distributed around the angle of specular direction. The other hand, specular diffractions are obsevered from vertical frame of windows. Figure 6 shows the elevation angle of the arrival wave. It can be seen that the value of elevation angle is around 0° for those arrival waves coming from glass/frame and bricks-I scatterers. It implies that most of the scattered waves from the building surface are arriving closely from specular directions. The diffraction effects are observed when the distance between transmitter and receiver antenna is 3.5–5 m with large elevation angle. It corresponds to the scattering point of specular diffraction from horizontal frame of windows. The arrival wave is specular ground-reflected wave when the angle of azimuth is −90°. Figure 6 shows that specular ground-reflected wave can not always be observed. This is possibly because the directivity of antenna toward the ground is rather small. Due to the antenna directivity the direct wave is more dominant. Therefore, the direct wave is observed in all measuring ranges. It is also possible that in Fig. 6, the elevation angle of specular ground-reflected wave approaches the elevation angle of the boundary between building and ground at distant points, so that the ground reflected wave might be classified as bricks II reflected waves. In the case of the first observation point located at 81.25 cm from the transmitter, six arrival waves were obtained, which consisted of two waves that arrive directly, one ground reflection and three waves from the building's surface. The reason why the two waves were directly obtained is because the distance between the transmitter and receiver is relatively close. Therefore, the receiver gets the reflection from the support of the antenna. This kind of result was only obtained at the first and second observation points.

5.2 Delay Times of Arrival Waves

Figure 7 shows power and delay time signal parameters for direct and ground reflected rays. This figure shows that the arrival waves scattered from the ground can be obtained if the distance between transmitter and receiver antenna is less

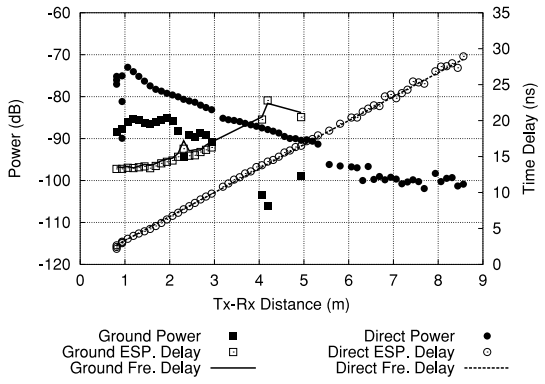

Fig. 7 Power and delay time of arrival wave for direct and ground reflection.

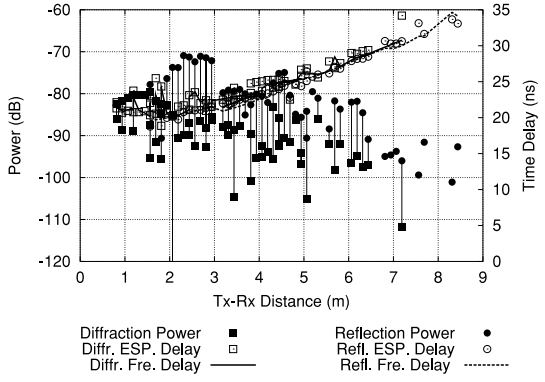

Fig. 8 Power and delay time of arrival wave for windows scatterer.

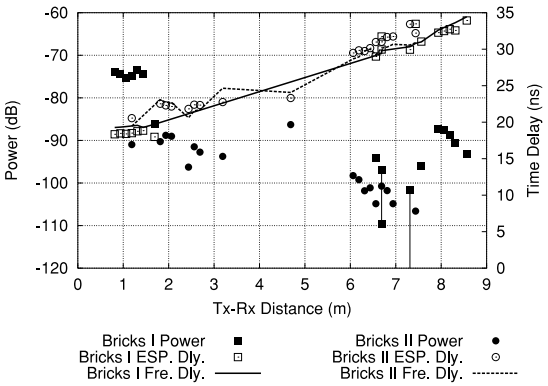

Fig. 9 Power and delay time of arrival wave for bricks scatterer.

Table 2 Average difference of experiment delay time with geometrical ray tracing delay time.

Type of Scatterer	Difference
Direct	0.25 ns
Ground Reflection	0.38 ns
Bricks I	0.83 ns
Bricks II	0.51 ns
Glass	0.62 ns

than 500 cm. It can be seen that each observation point receives the arrival waves coming directly from the transmitter. Figure 8 shows power and delay time for windows scattered rays. This figure shows that more than one scattered wave from glass was found from every observation point. This is due to the refractory properties of the glass material and the window shape with higher roughness. The parameters of the glass scatterer's arrival wave have a particular characteristic, i.e., when the observation point was close to the transmitter, the azimuth angles of the two arrival waves were varied at similar elevation angle, in contrast to similar azimuth angle but different elevation angle when the observation point was at a distant point from the transmitter. Average deviation of the angle is 12° for both cases. It means, that when the observation point is near the transmitter, the arrival waves were scattered at the vertical frame of windows, and when the observation point is at a distant, the arrival waves were scattered at the horizontal frame of windows. The figure also shows that power of specular reflected waves and diffracted waves are significantly different. Figure 9 shows power and delay time for the rays scattered by bricks rays. The figure shows that the power difference between bricks I and bricks II is significant enough compared to their time delay difference in spite of the same material. The second order scattering was discovered when the signal has low power and large delay time. Figures 8 and 9 clarify that non-specular scattering from the building surface is dominated more by window scatterers than by brick scatterers. Figures 7, 8 and 9 show that the delay time directly estimated by using ESPRIT yields close agreement with the delay time estimated by using propagation path based on free space velocity. It means that the classification of scatterer type shown in Figs. 5 and 6 is valid. Table 2 shows the average of the difference between the delay time directly estimated by using ESPRIT and the delay time by using propagation path based on free space velocity. In the case of bricks and glass scatterers, the values are larger in comparison to others due to the occurrence of second order scattering.

A second model with different spatial scanning was also investigated (see Fig. 3). It was found that the DoA & ToA wave and profiles for scatterrers in the second model are similar to the first model. Hence, the specular direction of arrival wave from model I and II can be applied in estimating the reflection coefficient of the building's surface.

5.3 Reflection Coefficient Estimation

The surface reflection coefficient of the building can be estimated by using signal parameters of the arrival wave from the specular direction. The measured reflection coefficients were compared with the theoretical Fresnel reflection formulas for smooth surfaces and rough surfaces using scattering correction of the modified Gaussian rough surface.

Measurement loss can be expressed as follows:

$$TL = RC + G_t + G_r + 20\log_{10}\frac{\lambda}{4\pi d}, \tag{22}$$

where TL [dB] is total loss of the measurement, RC [dB] is

Table 3 Roughness and dielectric parameters for building surfaces.

Parameter	Bricks	Glass
Mean. of Surf. Thickness (cm)	1.5	14.66
STD of Surf. Height σ_h (cm)	0.267	2.31
Permitivity (ϵ_r)	4.44	5.0
Permeability (μ_r)	1.0	1.0
Conductivity (σ) (S/m)	0.01	0.1

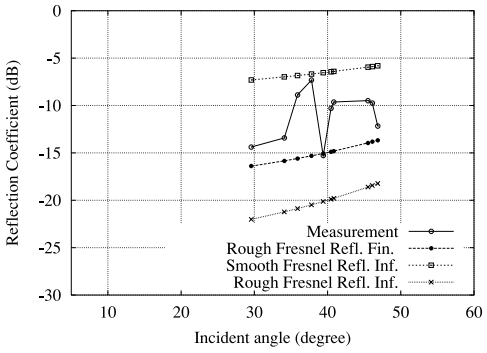

Fig. 10 Measurement and prediction of the glass reflection coefficient for model I.

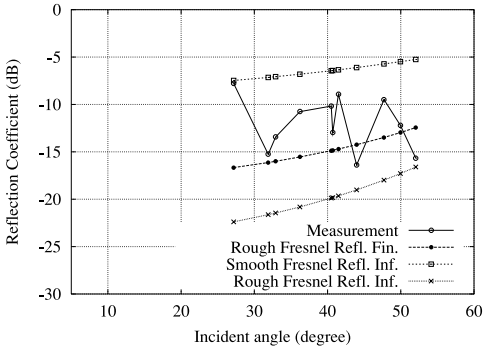

Fig. 11 Measurement and prediction of the glass reflection coefficient for model II.

reflection coefficient, G_t [dB] and G_r [dB], are directivities of the transmitter and the receiver antennas, respectively. Table 3 shows the estimate of surface roughness parameters and the measured dielectric properties of bricks, and the glass surface. Mean and standard deviation for surface height were obtained from surface height in the first fresnel zone for every arriving wave. Permitivity, permeability and conductivity of the material were obtained from [4].

5.3.1 Glass Surface Reflection Coefficient

Figures 10 and 11 show the reflection coefficient of the glass surface. These figures show that the reflection coefficients measurements for the glass surface are well bounded by the smooth and rough surface reflection coefficient prediction. The smooth surface of the Fresnel reflection coefficient of infinite thickness are applied using Eq. (4). On the other hand, rough surface of the Fresnel reflection coefficients of infinite thickness and finite thickness are applied by substituting Eq. (4) and Eq. (8) to Eq. (12), respectively. Figures 10 and 11 also show that the Fresnel reflection coefficient of finite thickness yields a better agreement with measured values compared with the others. Table 4 shows the average difference between predicted reflection coefficients and measured reflection coefficients.

Table 4 Average difference of predicted reflection coefficient with measured reflection coefficient for glass surface.

Model	Smooth Ref. Inf.	Rough Ref. Inf.	Rough Ref. Fin.
I	−4.57 dB	−8.91 dB	−3.91 dB
II	−5.70 dB	−7.59 dB	−3.59 dB

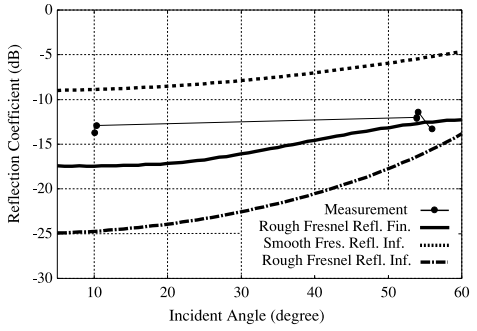

Fig. 12 Measurement and prediction of the bricks reflection coefficient for model I.

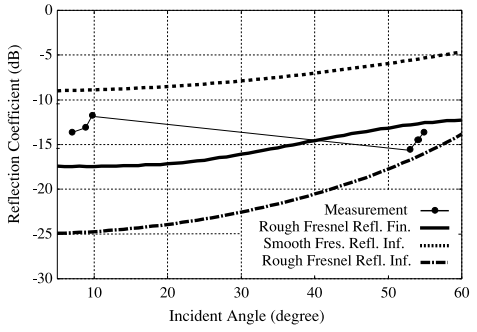

Fig. 13 Measurement and prediction of the bricks reflection coefficient for model II.

5.3.2 Bricks Surface Reflection Coefficient

In this section, bricks surface reflection coefficient is discussed. The reflection coefficients of bricks surface for model I and II are shown in Figs. 12 and 13, respectively. Both Figs. 12 and 13 explain that the measured reflection coefficients of the bricks surface are well bounded by the smooth and rough surfaces reflection coefficient prediction. The rough surface of the Fresnel reflection coefficient of finite thickness yields better agreement with the measured values when compared to the others. The averaged-differences for each predicted reflection coefficient with measured reflection coefficient are listed on Table 5. Table 6 presents the average and standard deviations of the measured reflection coefficient for glass and bricks surfaces. It is clarified that measured reflection coefficient of glass is

Table 5 Average difference of predicted reflection coefficient with measured reflection coefficient for bricks surface.

Model	Smooth Ref. Inf.	Rough Ref. Inf.	Rough Ref. Fin.
I	−5.90 dB	−6.87 dB	−3.79 dB
II	−6.13 dB	−7.25 dB	−5.17 dB

Table 6 Average and standard deviations of measured reflection coefficients for glass and bricks surfaces.

Model	Gls Mean	Gls STD	Brk Mean	Brk STD
I	−11.06 dB	2.61 dB	−12.68 dB	1.02 dB
II	−12.07 dB	2.91 dB	−13.30 dB	1.26 dB

more varied than for the bricks.

6. Conclusion

This paper presented the multipath characteristics of non-specular wave scattering from 3-D building surface roughness. The result shows that the multiple paths can be detected at many scatterers, such as ground, window's glass, window's frame, bricks surface, as well as directly from the transmitter. The signal parameters of the arriving waves from the building scatterer have a tendency to be distributed around the angle of specular direction. Maximum deviation of the angle is 20° in both azimuth and elevation. The delay time estimated by using ESPRIT result yields close agreement with the delay time estimated by using propagation path based on free space velocity The second order scattering was sometimes found with low power and large delay time. The non-specular scattering from building surfaces is more dominated by window scatterers than by brick scatterers. The glass and bricks reflection coefficients are well bounded by the theoritical Fresnel reflection formulas for smooth and rough surfaces using the scattering correction of the modified Gaussian rough surface. Moreover, the Fresnel reflection coefficient formula with thickness of the building surface and modified Gaussian scattering correction give better prediction in the glass and bricks surfaces measurement. The profile of the signal parameters between first period and second period of the building surface are similar.

Aknowledgement

The authors are really grateful to Professor H. Niiyama for the permission to use the GSIC-International Div. Tokyo Tech building for our experimental purpose. This work is partly supported by JSPS Scientific Research Grant-in-Aid.

References

[1] J. Takada, J. Fu, H. Zhu, and T. Kobayashi, "Spatio-temporal channel characterization in a sub-urban non-line-of-sight microcellular environment," IEEE J. Sel. Areas Commun., vol.20, no.3, pp.532–538, April 2002.

[2] H. Budiarto and J. Takada, "The effect of building surface roughness in mobile communication," Proc. Int. Symp. on Commun. Info. Tech.(ISCIT'01), pp.674–677, Thailand, 2001.

[3] L. Orlando, J.F. Martin, and T.S. Rappaport, "A comparison of theoretical and empirical reflection coefficients for typical exterior wall surfaces in a mobile radio environment," IEEE Trans. Antennas Propag., vol.44, no.3, pp.341–351, March 1996.

[4] K. Sato, H. Kozima, H. Masuzawa, T. Manabe. T. Ihara, Y. Kasashima, and K. Yamaki, "Measurements of reflection characteristics and refractive indices of interior construction materials in milimeter-wave bands," Proc. 45th IEEE Veh. Technol. Conf. (VTC'95) USA, pp.449–453, July 1995.

[5] A. Satoh and E. Ogawa, "An evaluation method for the reflection coeficient of buildings wall," Electron. Commun. Jpn. 1, Commun., vol.73, no.3, pp.92–103, 1990.

[6] K. Haneda, J. Takada, T. Iwata, and Y. Wakinaka, "Construction of a propagation path determination system for short range wireless communication system," Proc. The 3rd International Workshop on ITS Telecommunications 2002 (ITST 2002), pp.289–294, Seoul, Korea, Nov. 2002.

[7] M. Haardt and J.A. Nossek, "Simultaneous Schur decomposition of several nonsymmetric matrices to achieve automatic pairing in multidimensional harmonic retrieval problems," IEEE Trans. Signal Process., vol.46, no.1, pp.161–169, Jan. 1998.

[8] K. Sakaguchi, J. Takada, and K. Araki, "A novel architecture for MIMO spatio-temporal channel sounder," IEICE Trans. Electron., vol.E85-C, no.3, pp.436–441, March 2002.

[9] M.O. Al-Nuami and M.S. Ding, "Prediction models and measurements of microwave signals scattered from buildings," IEEE Trans. Antennas Propag., vol.42, no.8, pp.1126–1137, Aug. 1994.

[10] H.H. Xia, H.L. Bertoni, L.R. Maciel, A.L. Stewart, and R. Rowe, "Radio propagation characteristic for line-of-sight microcellular and personal communication," IEEE Trans. Antennas Propag., vol.41, no.10, pp.1439–1447, Oct. 1993.

Hary Budiarto was born in Surabaya-Indonesia in 1967. He received the B.Sc. degree in Mathematics from Sepuluh Nopember Institute of Technology, Surabaya-Indonesia, and the M.Sc. degree in Computer Science from University of Indonesia, Jakarta-Indonesia, in 1990 and 1998, respectively. Since May, 1992, he has been researcher in the Agency of the Assessment and Application Technology (BPP Teknologi) Jakarta-Indonesia. Presently, he is with Mobile Communication Group of Electrical & Electronic Engineering Dept., Tokyo Institute of Technology for pursuing his D.E. degree. His research interest are wireless propagation, signal processing, remote sensing and parallel processing. He received Young Researher's Encouragement Award from IEEE VTS Japan 2003. He is a student member of IEEE.

Kenshi Horihata was born in Kanagawa, Japan in 1980. He received the B.E.degree from Tokyo Institute of Technology, Japan, in 2003. His current interests are antenna and wireless propagation. He belongs to Panasonic Mobile Communications.

Katsuyuki Haneda was born in Kanagawa, Japan in 1979. He received the B.E. degree from Tokyo Institute of Technology, Japan, in 2002. His current interests are wireless propagation, channel modelling, array signal processing, and international development engineering. He is a student member of IEEE.

Jun-ichi Takada was born in Tokyo, Japan in 1964. He received the B.E., M.E., and the D.E. degrees from Tokyo Institute of Technology, Japan, in 1987, 1989, and 1992 respectively. From 1992 to 1994, he has been a Research Associate Professor at Chiba University, Chiba, Japan. From 1994, he has been an Associate Professor at Tokyo Institute of Technology, Tokyo, Japan. His current interests are wireless propagation and channel modelling, array signal processing, and ultra-wideband radio. He received the Excellent Paper Award and Young Engineer Award from IEICE, Japan, in 1993 and 1994, respectively. He is a member of IEEE, ACES, and AGU.